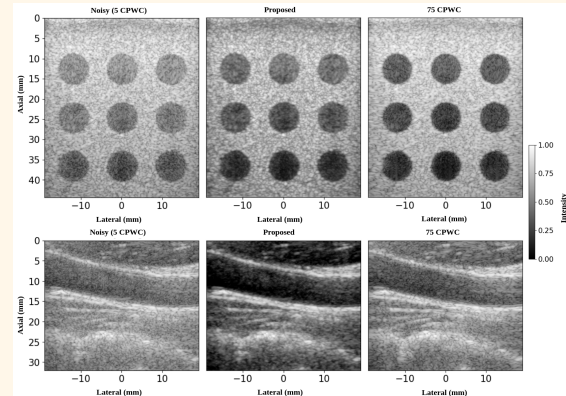


Lightweight Physics-Informed Zero-Shot Ultrasound Plane Wave Denoising

Hojat Asgariandehkordi*, Mostafa Sharifzadeh* and Hassan Rivaz, *Senior Member, IEEE*

Abstract—Ultrasound Coherent Plane Wave Compounding (CPWC) enhances image contrast by combining echoes from multiple steered transmissions. While increasing the number of angles generally improves image quality, it drastically reduces the frame rate and can introduce blurring artifacts in fast-moving targets. Moreover, compounded images remain susceptible to noise, particularly when acquired with a limited number of transmissions. We propose a zero-shot denoising framework tailored for low-angle CPWC acquisitions, which enhances contrast *without relying on a separate training dataset*. The method divides the available transmission angles into two disjoint subsets, each used to form compound images that include higher noise levels. The new compounded images are then used to train a deep model via a self-supervised residual learning scheme, enabling it to suppress incoherent noise while preserving anatomical structures. *Because angle-dependent artifacts vary between the subsets while the underlying tissue response is similar, this physics-informed pairing allows the network to learn to disentangle the inconsistent artifacts from the consistent tissue signal.* Unlike supervised methods, our model requires no domain-specific fine-tuning or paired data, making it adaptable across anatomical regions and acquisition setups. The entire pipeline supports efficient training with low computational cost due to the use of a lightweight architecture, which comprises only two convolutional layers. Evaluations on simulation, phantom, and *in vivo* data demonstrate superior contrast enhancement and structure preservation compared to both classical and deep learning-based denoising methods. The source code will be released at <http://code.sonography.ai> upon acceptance.

Index Terms—Ultrasound Plane Wave Compounding, Zero-Shot Denoising, Deep Learning.



I. INTRODUCTION

Ultrasound imaging, a non-invasive and cost-effective diagnostic modality, plays a vital role in modern clinical practice by enabling real-time visualization of internal anatomical structures and pathological conditions. Despite its advantages, such as safety, portability, and affordability, the quality of ultrasound images is often compromised by various types of noise, including speckle and artifacts caused by wave interactions with tissue heterogeneity [1]. These degradations can limit interpretability and reduce diagnostic confidence. As a result, the development of effective post-processing techniques has become essential to improve image clarity and diagnostic reliability [2], [3].

To overcome these challenges, early research on ultrasound

image enhancement focused on classical techniques such as spatial and frequency domain filtering, speckle reduction algorithms, and contrast enhancement strategies. While these methods have shown promise, they often fall short in addressing the complexity and variability of ultrasound data. This has motivated the exploration of more adaptive frameworks capable of dynamically adjusting to local image characteristics and structural content [4].

Recent advances in deep learning have led to significant improvements in medical image restoration, including ultrasound denoising. In particular, supervised Convolutional Neural Networks (CNNs) have demonstrated notable success in recovering clean images from noisy inputs. These models have been widely applied to tasks like speckle suppression, beamforming, and post-compounding enhancement in ultrasound. Their ability to learn complex mappings between noisy and clean domains has made them a compelling choice for data-driven image quality enhancement [2], [5]–[7].

However, supervised learning approaches face critical limitations. They rely on access to large-scale datasets with paired noisy and clean ground truth images. In ultrasound, such ground truth is typically unavailable as there is no

This work was supported by the Natural Sciences and Engineering Research Council of Canada (NSERC) and Fonds de recherche du Québec (FRQNT).

(Corresponding author: Hojat Asgariandehkordi.) Hojat Asgariandehkordi, Mostafa Sharifzadeh Hassan Rivaz are with the Department of Electrical and Computer Engineering, Concordia University, Montreal, QC H3G 1M8, Canada (e-mail: Hojat.Asgariandehkordi@mail.concordia.ca; mostafa.sharifzadeh@mail.concordia.ca; hrivaz@ece.concordia.ca).

*The authors contributed equally to this work.

Highlights

- **Introduces a zero-shot residual learning framework tailored to plane wave ultrasound, eliminating the need for training data.**
- **Achieves higher contrast and structural preservation across simulation, phantom, and *in vivo* datasets compared to supervised learning and classical baselines.**
- **Enables efficient training (even on CPU) using a compact network, broadening practical deployment in ultrasound diagnostics.**

standard “clean” reference image, particularly in patient data. Many studies resort to synthetic phantom acquisitions as solutions, which may not generalize to real-world scenarios. Moreover, these models often lack robustness across imaging domains. Variations in transducer hardware, anatomical regions, or imaging parameters can lead to domain shift, where the performance of a pre-trained model degrades significantly when applied outside its training distribution.

To mitigate the dependency on ground truth labels, the field has explored self-supervised learning approaches. These methods train denoising networks using only noisy data, often by masking parts of the input or leveraging spatial or temporal redundancy. Techniques such as Noise2Void, Noise2Self, and Neighbor2Neighbor eliminate the need for paired supervision by learning to predict a pixel from its local or global context [8]–[10]. Such frameworks have been adapted to ultrasound and other medical modalities, offering a more flexible alternative to the supervised pipelines [11]–[14].

Yet, self-supervised methods are not without limitations. While they remove the need for ground truth, they still require access to large and diverse datasets during training to learn meaningful noise-signal separation. As with supervised approaches, models trained on specific organs or imaging settings may struggle to generalize to unseen domains. This dependence on extensive data and persistent domain sensitivity reduces their practical applicability in settings with limited data availability or changing clinical conditions.

In contrast, zero-shot denoising offers a fundamentally different paradigm. These methods operate entirely on the test image, without requiring any training data. Pioneering examples include Zero-Shot Noise2Noise (ZS-N2N), which trains a lightweight network using spatially downsampled variants of the same noisy image [15]. Instead of relying on spatial downsampling, we exploit ultrasound physics. Specifically, we partition the available steering angles into two subsets, reconstruct two compounded images that share the same tissue response but exhibit distinct angle-dependent artifacts, and use these images as self-supervised pairs. This physics-informed pairing enables the network to learn, on the fly, to disentangle the consistent tissue signal from the inconsistent artifacts, thereby achieving effective zero-shot denoising without any external training data.

Despite their success in natural imaging, zero-shot methods have seen limited application in ultrasound, and even less so in the context of Coherent Plane Wave Compounding (CPWC). In this work, we propose a zero-shot denoising framework tailored for CPWC ultrasound images obtained with a limited number of transmission angles. Our method requires no training data, clean images, or prior noise mod-

eling. Instead, it leverages the angular diversity inherent in the CPWC acquisition by dividing the available angle set into two complementary subsets. Each subset is used to reconstruct a noisier compounded image. These two images are treated as pseudo-pairs for self-supervised residual learning. A lightweight CNN is trained directly using the pseudo-pairs to extract uncorrelated components. Once trained, the model estimates and subtracts noise from the original compounded image to yield a denoised, contrast-enhanced result. The main contributions of this paper are as follows:

- **Zero-shot CPWC denoising:** We tailor zero-shot denoising to the context of CPWC for the first time, enabling image enhancement without requiring any training data.
- **Customized downsampling:** We propose a domain-specific physics-informed angular sampling strategy that adapts the ZS-N2N framework to plane wave ultrasound imaging. The model is trained to disentangle inconsistent artifacts from consistent tissue signal.
- **Lightweight architecture:** We use a lightweight CNN model with only two convolutional layers, supporting efficient training even on conventional CPUs. This design reduces computational training overhead relative to conventional supervised and self-supervised approaches.
- **Extensive evaluation:** We perform a comprehensive evaluation on simulation, phantom, and *in vivo* ultrasound datasets, demonstrating consistent improvements in contrast metrics and perceptual image quality over both classical and deep learning-based denoising methods.

II. RELATED WORK

A wide range of techniques has been developed to address the denoising problem in ultrasound imaging, ranging from traditional signal processing filters to modern deep learning and self-supervised methods. In this section, we provide a review of related work across three main categories: classical denoising techniques, supervised deep learning-based models, and self-supervised learning strategies.

A. Classical Denoising Methods

Ultrasound imaging inherently suffers from speckle noise and artifacts due to acoustic wave interactions with tissue structures. Traditional denoising methods including spatial filters, anisotropic diffusion, wavelet transforms, and Non Local Means (NLM) have been widely used to suppress such degradations by leveraging statistical and spatial redundancies [16]. Among them, NLM is notable for preserving anatomical details through patch-based averaging, but it

remains computationally intensive and sensitive to parameter tuning. Similarly, BM3D-based approaches, such as the brushlet-enhanced method by Gan *et al.* [17], improve noise suppression but exhibit comparable sensitivity to parameters and computational complexity.

Beam steering has been used to enhance the quality of elastography [18] and speckle characterization [19]. Advanced classical methods leverage signal coherence in steered angles to improve ultrasound imaging. In CPWC [18], post-beamforming coherence-based filters such as the coherence factor [20], generalized coherence factor [21], and their statistical variants [22], [23] enhance image quality by promoting phase-aligned signals and suppressing incoherent components. These methods are particularly effective in reducing sidelobe artifacts in beamformed images.

Despite these advancements, classical models remain limited by their heuristic nature, parameter sensitivity, lack of data adaptivity, and computational complexity. Many require careful tuning for specific imaging setups and often underperform in diverse or complex scenarios. Additionally, they often degrade important structural information. These limitations have motivated the rise of deep learning approaches, which offer greater flexibility and higher-quality denoising with significantly reduced inference cost.

B. Supervised Deep Learning-based Denoising Methods

Deep learning has become foundational in advancing plane wave ultrasound imaging, particularly in tasks such as beamforming, denoising, and reconstruction from sparsely acquired data [11], [24], [25].

Early supervised architectures such as the multichannel, multiscale CNN proposed by Zhou *et al.* successfully reconstructed high spatial-temporal resolution plane wave images by combining multi-angle data and cascading wavelet filters [26]. Nguon *et al.* extended this line of work with a modified U-Net beamformer adapted to multiple imaging conditions through transfer learning [27]. Goudarzi and Rivaz demonstrated that CNNs trained on simulated (Radio Frequency) RF data generalized effectively to *in vivo* images [28]. A CNN beamformer combining GoogLeNet and U-Net was proposed in [29] to reconstruct a high-quality ultrasound image using a single-angle plane wave input. Perdios *et al.* [30] trained an adapted version of U-Net on simulation data and showed that their network also performs well on *in vivo* data. Gupta *et al.* [31] looked at image denoising as an inverse problem and solved it using a deep learning model. A network called Mimicknet [32] was proposed to improve image quality in post-beamformed data. Van Sloun *et al.* [4] have explored deep learning methods that have been developed for adaptive beam-forming, spectral doppler, clutter suppression, and super-resolution.

Compared to natural images, ultrasound data present unique difficulties due to their low contrast and broad dynamic range [33]. These characteristics complicate the direct application of CNNs for image enhancement across various ultrasound tasks. To overcome these challenges, researchers have explored a combination of pre-processing strategies and

network designs. The Mean Signed Logarithmic Absolute Error (MSLAE) was introduced as a specialized loss function within a residual CNN framework incorporating multiscale, multichannel filters [34]. For high-frequency signal recovery, wavelet-based multi-resolution networks have also been proposed [28]. Additionally, to avoid convergence to poor local optima in the early training stages, caused by rapid RF fluctuations, a hybrid loss function was designed that adaptively shifts from B-mode loss to RF-domain loss throughout the training [11].

Generative Adversarial Networks (GANs) have further elevated perceptual image quality. Zhou *et al.* introduced an ultrasound-transfer GAN to approximate line-scan quality from plane wave inputs [35], Tang *et al.* combined adversarial training with attention mechanisms to recover fine anatomical details [36], and Goudarzi *et al.* applied GANs for multi-focus reconstruction [37].

Recent attention has shifted toward probabilistic generative models known as Denoising Diffusion Probabilistic Models (DDPMs) [38] represent a new paradigm in learning the distributions. DDPMs use a noise reversal process to recover high-fidelity outputs. Enhanced DDPMs have addressed issues like slow sampling [39], limited expressivity [40], and high memory cost [41], [42].

In ultrasound, DDPMs have been leveraged for denoising and super-resolution. Asgariandehkordi *et al.* trained a DDPM on CPWC data with angular diversity to isolate incoherent noise and recover clean structure [24]. Liu *et al.* proposed a diffusion-based super-resolution pipeline for ultrasound [43], while Zhang *et al.* demonstrated denoising from under-sampled plane wave inputs using learned priors [44]. In [1], a diffusion model was employed for ultrasound cardiography dehazing. Two diffusion models were trained to generate a patch-wise clean image and haze separately using a hazy image as a condition. A diffusion model was proposed in [45] to reconstruct high-quality 3D ultrasound from sparsely sampled elevation planes, outperforming conventional and deep learning interpolators. Chen *et al.* proposed a latent dynamic diffusion model to synthesize realistic ultrasound videos from static images, enhancing video classification performance and addressing the scarcity of labeled ultrasound video datasets [46]. Dominguez *et al.* introduced a physics-based diffusion model tailored for ultrasound imaging, incorporating a custom scheduler that simulates acoustic wave propagation to generate more realistic synthetic data [47].

Although effective, these methods depend on clean training data, which is often unavailable in ultrasound, and tend to be computationally complex. For example, some diffusion-based methods can only perform offline processing even on powerful GPUs [1], highlighting the need for faster methods [48]. Self-supervised models address the reliance on paired clean data by learning directly from noisy inputs without ground truth, which are discussed in the next section.

C. Self-Supervised Methods

Noise2Noise [49] demonstrated that denoising networks can be trained using only pairs of independently corrupted images,

eliminating the need for clean targets by leveraging the statistical independence of noise. This method showed that learning to map one noisy image to another could still lead to effective noise suppression. Building on this work, self-supervised denoising methods often rely on strategies like masking, random corruption, or predicting pixels based on their surroundings. For example, Noise2Void and Noise2Self [8], [9] hide certain pixels and train the network to predict their values using neighboring pixels, assuming that nearby pixels share similar information while noise is random. Neighbor2Neighbor [10] extends this idea by identifying pairs of nearby pixels that are likely to share the same underlying structure and using them to train the network.

However, many of these approaches were developed for natural or biomedical microscopy images, which often differ significantly from ultrasound data in terms of noise characteristics and image formation physics. Ultrasound images exhibit speckle, coherent artifacts, and depth-dependent attenuation, all of which challenge generic self-supervised assumptions. Thus, domain-specific adaptations are necessary for successful ultrasound denoising. Therefore, several self-supervised approaches have emerged. Zhang *et al.* [50] aimed to reconstruct high-quality ultrasound plane waves from raw channel data by training a self-supervised network in an inverse problem approach. Sharifzadeh *et al.* [11] introduced an aberration correction strategy, where the network was trained using pairs of images that shared structural content but differed in aberration. This approach allowed the model to learn to suppress aberration artifacts without requiring clean ground truth images by leveraging the variability in the aberrated inputs. A deblurring-based masked image modeling framework was proposed in [51] to improve ultrasound image representation learning by leveraging its high noise-to-signal ratio, achieving state-of-the-art performance on classification and segmentation tasks.

One promising approach is Deep Coherence Learning [13], which eliminates the need for paired noisy-clean training data by enforcing coherence constraints between multiple plane waves, improving image quality while maintaining high frame rates. Despite its advantages, this method necessitates training data that closely matches the domain of the inference data, limiting its effectiveness under new imaging conditions, transducers, or anatomical structures that were not well-represented during training. Additionally, it requires multi-day GPU training, as reported in their study.

Zero-shot denoising eliminates the need for pre-collected training datasets by leveraging the intrinsic properties of noisy images to perform self-consistent denoising. The ZS-N2N framework [15] has demonstrated that noise removal can be performed without access to high-quality images, making it particularly suitable for applications where acquiring high-quality ground truth is infeasible. In this work, we adapt ZS-N2N to ultrasound plane wave denoising; our approach considers low-angle compounded images as inherently noisy and enhances their quality by leveraging self-supervised learning. Without requiring external supervision, it efficiently suppresses noise, offering a robust and data-efficient denoising solution.

The rest of the paper is designed as follows. The proposed method is described in Section III. Then, the experimental setups, datasets, evaluation metrics, and training strategy are detailed in Section IV, followed by the comparison results in V. The discussions are in Section VI, and the paper is concluded in Section VII.

III. METHODS

We propose a zero-shot denoising framework for CPWC images by leveraging the angular diversity inherent in the acquisition process. Specifically, a compounded image y , formed from a low number of transmissions, is decomposed into two subsets: one constructed using odd-indexed angles and the other using even-indexed angles (Fig. 1). Each subset yields a compounded image with increased noise levels as a result of diminished angular compounding.

A lightweight CNN f_θ is subsequently trained on this pair using a combination of symmetric residual and consistency loss functions. The training process encourages the network to learn incoherent components, primarily noise and artifacts, between the two inputs. Since the original image y is composed of both subsets, the trained network can estimate the noise residuals present in y and subtract them, resulting in an enhanced image with improved contrast and reduced noise.

1) *Image Downsampling*: CPWC consists of a set of different steering angles, denoted as $\{P_1, P_2, \dots, P_k\}$, where k represents the number of transmissions over a range of $-N^\circ$ to $+N^\circ$. To construct training pairs, we define two sampling functions, $S_1(\cdot)$ and $S_2(\cdot)$, which extract disjoint subsets of the available angles:

$$S_1(y) = \{P_i \mid i \in \mathcal{I}_1\}, \quad S_2(y) = \{P_j \mid j \in \mathcal{I}_2\}, \quad (1)$$

where \mathcal{I}_1 and \mathcal{I}_2 are non-overlapping index sets (e.g., odd and even indices). The two resulting compounded images, $S_1(y)$ and $S_2(y)$, serve as inputs to the network. Although each is individually noisy, they share a common anatomical structure while differing in artifacts. This enables the model to learn angle-dependent artifacts directly from the input without requiring any external supervision or clean reference data.

2) *Plane Wave Denoising*: Given a plane wave image y , the proposed approach involves training a lightweight network f_θ to estimate the discrepancies between two sampled subsets. By learning the relationship between $S_1(y)$ and $S_2(y)$, the network disentangles correlated anatomical structures from the artifacts, thereby enhancing the original noisy plane wave image. A baseline loss function for this mapping is as follows:

$$L = \|f_\theta(S_1(y)) - S_2(y)\|_1, \quad (2)$$

where $\|\cdot\|_1$ denotes L_1 norm. Once trained, the network can be directly applied to denoise the original compounded image using $x = f_\theta(y)$, where x denotes the denoised output. However, experimental evidence suggests that residual learning provides more effective noise suppression [52]. Instead of directly predicting the clean image, the network is trained to

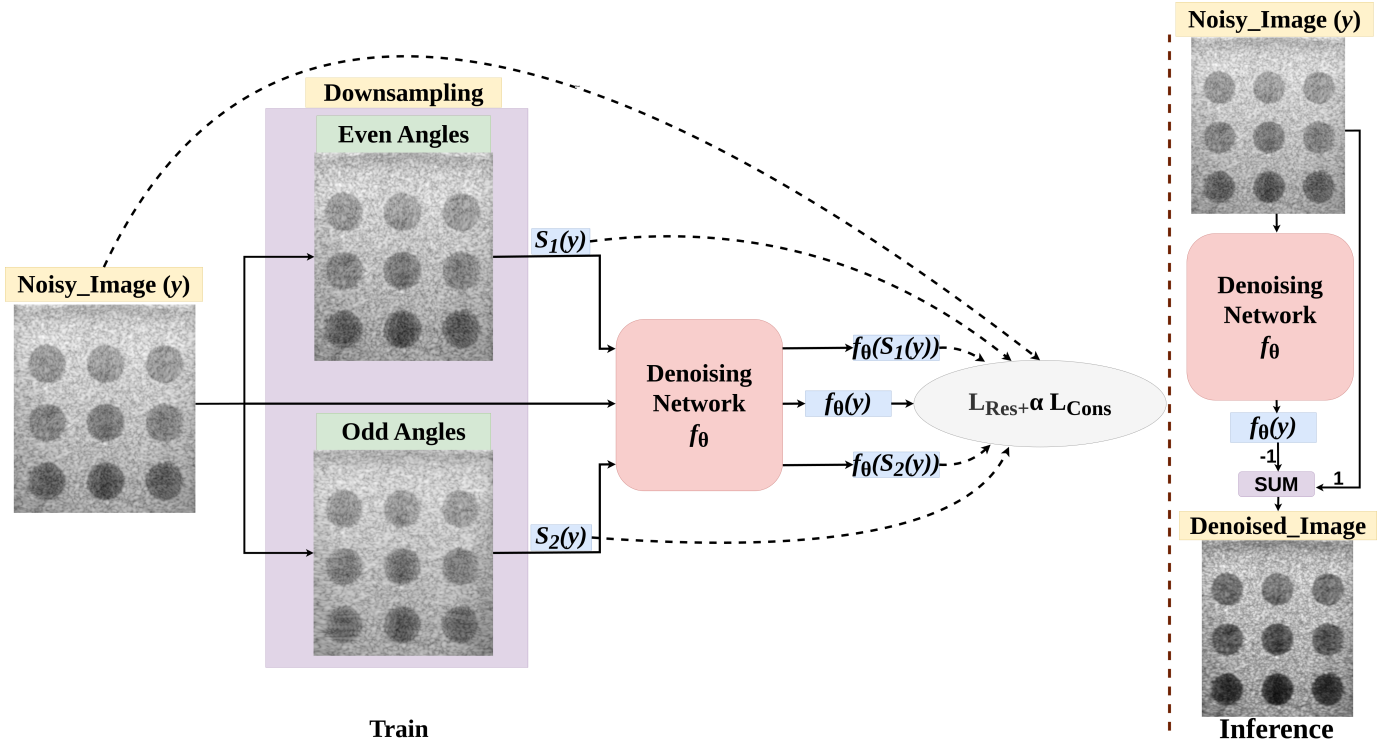


Fig. 1. An overview of the proposed method. A low-compounding plane wave image y is decomposed into even-angle $S_1(y)$ and odd-angle $S_2(y)$ subsets. A lightweight network f_θ is trained using a combined residual and consistency loss function ($L_{\text{Res}} + \alpha L_{\text{Cons}}$) to learn noise characteristics. Once trained, in the inference phase, the network estimates and removes the noise component from y , producing a denoised output.

estimate the noise residual and subtract it from the input. The corresponding residual formulation is:

$$L = \|S_1(y) - f_\theta(S_1(y)) - S_2(y)\|_1. \quad (3)$$

Inspired by symmetric training strategies in self-supervised representation learning [53], we adopt a symmetric residual loss that enforces bidirectional consistency between the two downsampled images:

$$L_{\text{Res.}} = \frac{1}{2} \left(\|S_1(y) - f_\theta(S_1(y)) - S_2(y)\|_1 + \|S_2(y) - f_\theta(S_2(y)) - S_1(y)\|_1 \right). \quad (4)$$

3) Consistency Loss: To ensure that the denoised image remains structurally faithful to the original domain and to mitigate over-smoothing, we introduce a gradient-based consistency loss function. This loss encourages the gradient of the denoised image to match the gradient of the original input image y , helping to preserve important edge and texture information.

However, directly using ∇y as a reference may propagate high-frequency noise into the loss, as the gradient operator amplifies noise. To address this, we replace ∇y with its smoothed version, obtained by convolving y with a Gaussian kernel G_σ followed by the gradient operator. The consistency loss is then defined as:

$$L_{\text{Cons.}} = \|\nabla(y - f_\theta(y)) - \nabla(G_\sigma * y)\|_1, \quad (5)$$

where $*$ denotes convolution and G_σ is a Gaussian filter.

4) Total Loss Function: The final training loss is expressed as follows:

$$L_{\text{Total}} = L_{\text{Res.}} + \alpha \cdot L_{\text{Cons.}}, \quad (6)$$

where α is the consistency loss coefficient. We train the proposed method using L_{Total} . After training, the network is used to denoise the original noisy plane wave image by computing:

$$x = y - f_\theta(y), \quad (7)$$

where x denotes the final denoised image.

IV. EXPERIMENTS

This section begins by describing the datasets used for evaluation. Subsequently, the implementation details are outlined, followed by a description of the evaluation metrics employed to quantify performance.

A. Datasets

We evaluate the proposed method on a diverse range of datasets comprising simulation, phantom, and *in vivo* acquisitions. This collection is specifically curated to support standardized assessment of ultrasound beamforming and denoising algorithms, ensuring both fair comparisons and reproducibility across future studies.

1) Simulation Contrast: Image containing anechoic cysts (from PICMUS dataset [54]) arranged horizontally and vertically within a fully developed speckle background, specifically designed to evaluate contrast performance.

2) *Experimental Phantom*: This data consists of two anechoic cylinders and was collected using an L11-5v linear array transducer operated with a Vantage 256 system (Verasonics, Kirkland, WA) to scan a multi-purpose, multi-tissue ultrasound phantom (Model 040GSE, CIRS, Norfolk, VA).

3) *in vivo*: The image of the longitudinal (denoted as Carotid Longitudinal, CL) and cross-sectional views (denoted as Carotid Cross-sectional, CC) of the carotid artery from a healthy volunteer (from PICMUS dataset [54]).

B. Implementation Details

The proposed framework was implemented in PyTorch and trained on log-compressed B-mode images reconstructed using Delay-and-Sum beamforming. Although the method is compatible with beamformed (RF) data, we opted for B-mode images due to their wider accessibility, thereby enhancing practicality for implementation and reproducibility. We used a lightweight convolutional architecture consisting of only two 3×3 convolutional layers with 48 channels, each followed by a Leaky ReLU activation function (negative slope = 0.2), and a final convolution 1×1 for refinement of the characteristics. The total parameter count is under 22k, making the network highly efficient. Training was performed using stochastic gradient descent (SGD) with an initial learning rate of 0.001. The model was optimized over 1000 iterations for each test image in a zero-shot manner using a single NVIDIA RTX 4090 GPU. All experiments were conducted using five steering angle compounding ($k = 5$ and $N = 16$) as the original input, and the consistency loss coefficient α was heuristically set to 0.25 and G_σ is a 3×3 Gaussian filter.

C. Evaluation Metrics

We quantitatively evaluated the performance of our method using three metrics: Contrast-to-Noise Ratio (CNR), generalized Contrast-to-Noise Ratio (gCNR) [55], and Kolmogorov–Smirnov (KS) test.

1) *Contrast-to-Noise Ratio (CNR)*: CNR quantifies the separation between the Region Of Interest (ROI) and the background by measuring the ratio of their mean intensity difference to the combined noise level. It is computed as:

$$\text{CNR} = 20 \log_{10} \left(\frac{|\mu_{\text{ROI}} - \mu_B|}{\sqrt{\frac{\sigma_{\text{ROI}}^2 + \sigma_B^2}{2}}} \right), \quad (8)$$

where μ and σ represent the mean and standard deviation of the ROI and background regions, respectively.

2) *Generalized Contrast-to-Noise Ratio (gCNR)*: As CNR can be sensitive to dynamic range scaling [55], gCNR was introduced to address this limitation. It is defined as:

$$\text{gCNR} = 1 - \int_{-\infty}^{\infty} \min\{p_{\text{ROI}}(x), p_B(x)\} dx, \quad (9)$$

where p_{ROI} and p_B are the intensity histograms of the ROI and background. gCNR measures the degree of histogram overlap between regions, with values closer to 1 indicating a clearer separation.

3) *Kolmogorov-Smirnov (KS) Test*: To evaluate speckle preservation, we use the KS test to compare the cumulative distribution functions of pixel intensities between the processed and original images. This test is sensitive to deviations from the characteristic Rayleigh distribution observed in speckle-dominated regions.

V. RESULTS

We compare our results with classical, supervised and zero-shot approaches. For the classical baselines, we include BM3D [17]. For the supervised baselines, we trained MSLAE [34] and DPWDPM [24] using the simulation dataset from [24]. It is worth noting that because the supervised methods were specifically developed for RF images, we had to train them on RF data and then use the B-mode version of their outputs in the comparisons. For the zero-shot baseline, we compare to ZS-N2N [15]. For quantitative evaluation, we use CNR, gCNR, KS test, as described in Section IV-C. Visual comparisons are also included to highlight improvements in contrast and speckle preservation. All visual results are in B-mode, shown using a dynamic range of -80 dB, normalized to the $[0, 1]$ range for consistency. In all of the quantitative and visual results, 5 CPWC stands for compounding with 5 steering angles, and 75 CPWC stands for compounding with 75 steering angles.

1) *Simulation Results*: To evaluate denoising performance in controlled settings, we used simulated cyst phantom data. The contrast performance is quantified using gCNR and CNR metrics. The cyst ROIs and background areas used for these measurements are indicated in Fig. 2 using green and red circles, respectively.

Table I reports CNR and gCNR values averaged across three rows of cysts at increasing depths. Five methods are compared: a classical (BM3D), a zero-shot (ZS-N2N), two supervised (MSLAE and DPWDPM) denoising methods, and the proposed method. KS test results are also included to ensure statistical consistency post-denoising.

The proposed method consistently achieves top-tier contrast across all depths. In Row 1, it yields the highest CNR (3.7) and gCNR (0.89), outperforming all baselines, including BM3D CNR (3.5) and DPWDPM CNR (2.9). At mid-depth (Row 2), it maintains strong performance with CNR (4.4) and gCNR (0.97). In deeper regions (Row 3), it again leads with the best gCNR (0.99) and a high CNR (5.4). While DPWDPM performs competitively at depth, it exhibits structural artifacts visible in the visual comparison. All methods pass the KS test, confirming distributional alignment between input and output intensities.

Fig. 2 provides qualitative comparisons. Our method enhances contrast and preserves fine structural details while avoiding the blurring or artifacts present in competing techniques. A zoomed-in view shows the visual gain achieved compared to the noisy input (5 CPWC), bringing our result closer to the high-quality 75 CPWC reference.

As for the runtime, for the image in Fig. 2 with a size 300×384 , our method takes 6 seconds (which includes both training and inference). For the same image, BM3D and ZS-N2N take

1 and 3 seconds, respectively. DPWDPM and MSLAE, which are applied to RF image of size 1200×384 , take 1.2 and 0.2 seconds (for inference only), respectively. Our method is not currently optimized for speed; in the VI section (Discussion section), we will outline strategies to substantially accelerate it.

TABLE I

QUANTITATIVE RESULTS ON SIMULATED TEST IMAGES. THE CONTRAST METRICS ARE AVERAGED ACROSS EACH ROW OF CYSTS.

Method	Row	Mean gCNR (\uparrow)	Mean CNR (dB) (\uparrow)	KS Test
Noisy Image	1	0.67	2.9	passed
	2	0.77	3.0	
	3	0.80	3.6	
BM3D [17]	1	0.80	3.5	passed
	2	0.89	3.9	
	3	0.94	4.4	
ZS-N2N [15]	1	0.73	2.8	passed
	2	0.83	3.3	
	3	0.87	3.9	
MSLAE [34]	1	0.68	2.8	passed
	2	0.77	3.3	
	3	0.82	3.9	
DPWDPM [24]	1	0.82	2.9	passed
	2	0.95	5.3	
	3	0.91	4.5	
Proposed	1	0.89	3.7	passed
	2	0.97	4.4	
	3	0.99	5.4	
75 CPWC	1	0.98	5.7	passed
	2	0.98	5.8	
	3	0.99	6.1	

2) Phantom Results: The phantom dataset consists of two cysts: Cyst 1 located near the transducer and Cyst 2 at a greater depth. To compute CNR and gCNR, circular masks were applied to define ROI and background regions, as illustrated in Fig. 3, with green indicating the ROI and red the background. The proposed method delivers cleaner cyst boundaries and enhanced contrast, particularly in deeper regions. Unlike supervised or zero-shot baselines, it introduces minimal smoothing or structural artifacts.

Quantitative contrast metrics are summarized in Table II. The 75 CPWC image serves as the high-quality reference, with Cyst 1 yielding gCNR (0.91) and CNR (3.4), and Cyst 2 reaching gCNR (0.82) and CNR (2.8). These values establish the baseline for comparison.

As for the zero-shot methods, BM3D and ZS-N2N performed reasonably well. BM3D achieved gCNR (0.78) and CNR (2.4) for Cyst 1, but failed to significantly enhance deeper regions. ZS-N2N had comparable gCNRs (0.76) and achieved its highest CNR (3.0) at depth, but it produced only marginal visual improvement and left residual noise.

The supervised models (MSLAE and DPWDPM) delivered moderate scores. MSLAE's performance degraded with depth, while DPWDPM achieved slightly better contrast (Cyst 2: gCNR = 0.83, CNR = 2.4), though still with observable structural artifacts.

The proposed zero-shot model yielded the most consistent performance across depths. For Cyst 1, it reached gCNR (0.90) and CNR (3.1), which is competitive with all baselines. In the deeper Cyst, it achieved gCNR (0.86) and CNR (2.7), nearly matching the 75 CPWC reference and exceeding all other methods. All methods passed the KS test, indicating that the noise distributions were statistically preserved post-denoising.

TABLE II

QUANTITATIVE RESULTS ON PHANTOM IMAGES. CONTRAST METRICS ARE REPORTED FOR EACH CYST.

Method	Cyst	gCNR (\uparrow)	CNR (dB) (\uparrow)	KS Test
Noisy Image	1	0.75	2.1	passed
	2	0.75	2.0	
BM3D [17]	1	0.78	2.4	passed
	2	0.78	2.3	
ZS-N2N [15]	1	0.76	2.1	passed
	2	0.76	3.0	
MSLAE [34]	1	0.76	2.3	passed
	2	0.74	2.1	
DPWDPM [24]	1	0.78	2.1	passed
	2	0.83	2.4	
Proposed	1	0.90	3.1	passed
	2	0.86	2.7	
75 CPWC	1	0.91	3.4	passed
	2	0.82	2.8	

3) *in vivo* results: To assess the clinical utility of our method, we evaluated it on two *in vivo* scans: CL and CC. These images capture vascular anatomy embedded in tissue with moderate to low contrast, representative of real-world diagnostic conditions. We report both quantitative and qualitative comparisons with classical, supervised, and zero-shot baselines.

a) CL Dataset: Table III presents the gCNR and CNR metrics for the CL data. The ROI and background regions, used for computing these metrics, are shown in Fig. 4 in green and red, respectively. Our proposed method achieved the highest performance with a gCNR (0.87) and a CNR (3.0), outperforming the classical methods such as BM3D (0.80, 2.6), zero-shot ZS-N2N (0.80, 2.4), and supervised baselines like MSLAE (0.79, 2.0) and DPWDPM (0.80, 2.4). Notably, our model also surpassed the 75-angle CPWC reference image (0.83, 2.7), demonstrating the effectiveness of the zero-shot approach.

Qualitative results in Fig. 4 further support these findings. The proposed method retains clear vessel wall boundaries and anatomical detail, while the other methods suffer from artifacts.

TABLE III

QUANTITATIVE RESULTS ON THE *in vivo* CL DATA. THE ROI AND THE BACKGROUND REGIONS ARE SHOWN IN FIG. 4.

Method	gCNR (\uparrow)	CNR (dB) (\uparrow)	KS Test
Noisy Image	0.79	2.3	passed
BM3D [17]	0.80	2.6	passed
ZS-N2N [15]	0.80	2.4	passed
MSLAE [34]	0.79	2.0	passed
DPWDPM [24]	0.80	2.4	passed
Proposed	0.87	3.0	passed
75 CPWC	0.83	2.7	passed

b) CC Dataset: Table IV summarizes the denoising performance on the CC dataset. The ROI and background masks used for contrast evaluation are displayed in Fig. 5. Consistent with the trend observed in CL, the proposed method achieved the best gCNR value (0.80) and tied for the top CNR (2.3), matching the 75 CPWC compound reference and surpassing all other methods.

The visual results in Fig. 5 highlight the ability of our

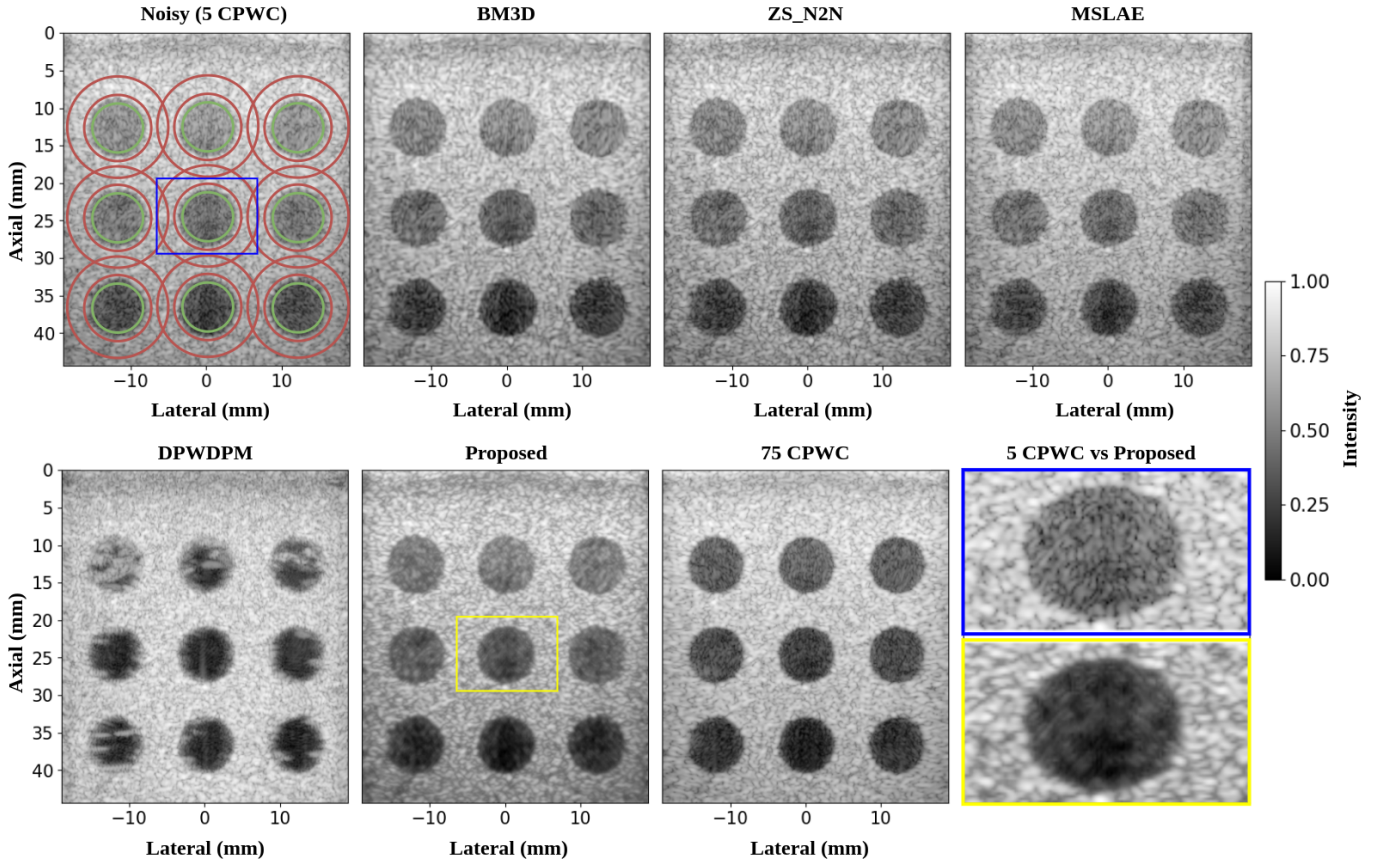


Fig. 2. Visual comparison of the simulation results. All images are displayed with a dynamic range of -80 dB normalized to $[0, 1]$. The green and red regions indicate the ROI and the background areas, respectively. The zoomed-in images correspond to the blue and yellow rectangles in the noisy image (5 CPWC) and the proposed method, respectively.

approach to suppress noise while retaining detailed structure in deeper tissues. Competing methods like BM3D and ZS-N2N exhibit minor improvements, and supervised approaches tend to introduce additional artifacts attributable to domain shift between the input CC data and the data used to train their models. In contrast, the proposed method performs training and testing on the same image, thereby circumventing the domain shift problem and achieving effective denoising while preserving sharp anatomical structures. All methods passed the KS test on both datasets, indicating that the denoising process did not distort the statistical characteristics of background noise.

TABLE IV

QUANTITATIVE RESULTS ON THE *in vivo* CC DATA. THE ROI AND THE BACKGROUND REGIONS ARE SHOWN IN FIG. 4.

Method	gCNR (\uparrow)	CNR (\uparrow)	KS Test
Noisy Image	0.74	2.1	passed
BM3D [17]	0.76	2.2	passed
ZS-N2N [15]	0.78	2.3	passed
MSLAE [34]	0.74	2.1	passed
DPWDPM [24]	0.71	2.0	passed
Proposed	0.80	2.3	passed
75 CPWC	0.78	2.3	passed

VI. DISCUSSION

This study introduces a zero-shot self-supervised denoising method tailored for plane wave ultrasound imaging. Unlike most existing deep learning approaches that require either paired datasets or large-scale training data, our method leverages a physics-inspired angle-based self-supervision strategy. This allows it to *learn directly from the noisy test image* without the need for training data.

Quantitative and qualitative results across simulation, phantom, and *in vivo* datasets demonstrate the robustness and generalizability of the proposed zero-shot denoising framework. In simulation experiments, the method consistently outperforms baselines that do not require a dedicated training dataset, such as BM3D and ZS-N2N, in both gCNR and CNR metrics across all cyst depths. Compared to supervised models such as MSLAE and DPWDPM, which were trained on synthetic datasets, the proposed approach achieves superior contrast without introducing artifacts, particularly in deeper regions where conventional methods encounter limitations due to lower SNR.

In phantom experiments, which introduce real-world attenuation and speckle characteristics, the proposed approach again delivers strong performance. While BM3D performs reasonably well in shallow cysts, it tends to oversmooth deeper structures. In contrast, our method achieves the highest

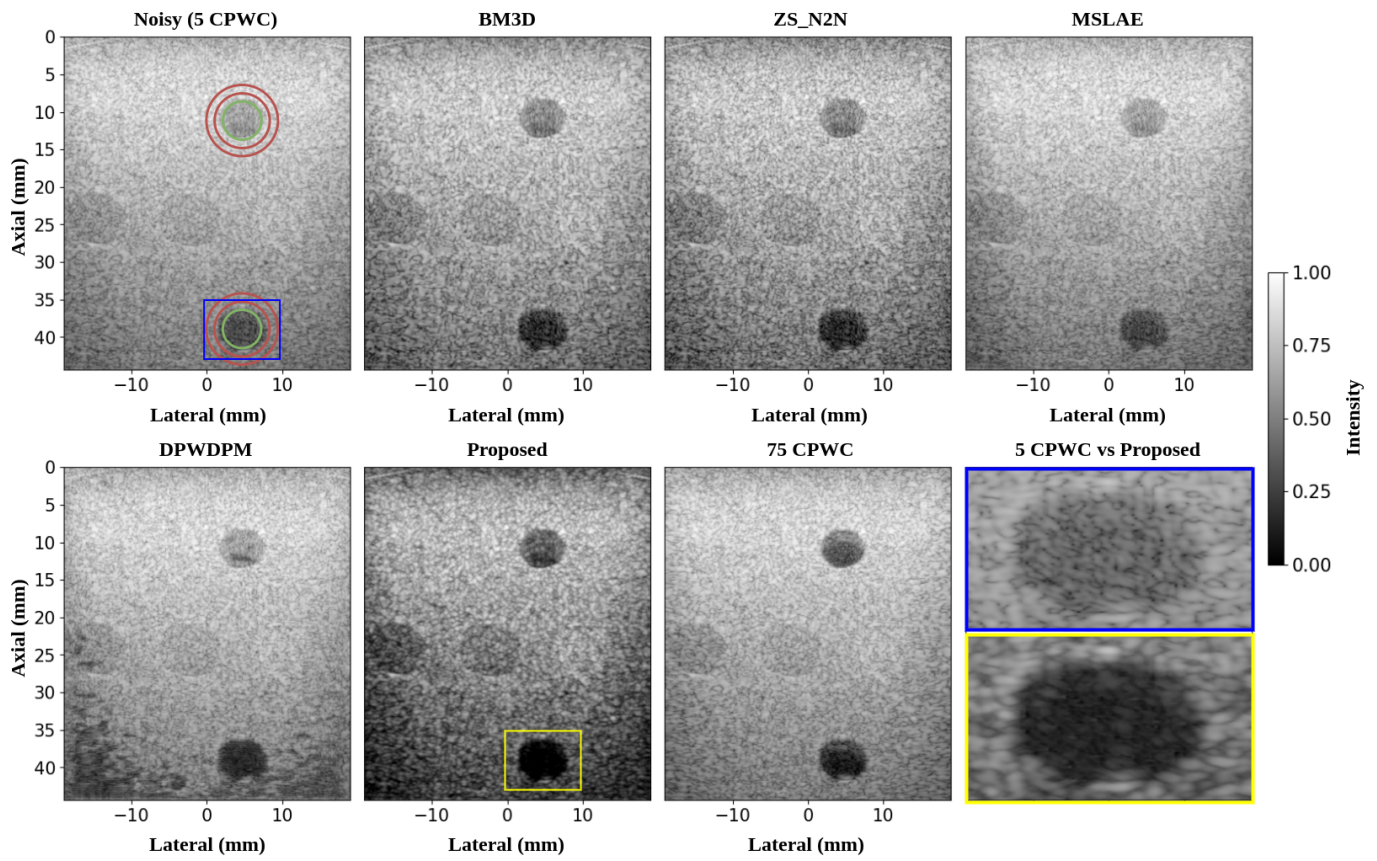


Fig. 3. Visual comparison on the phantom data. All images are displayed with a dynamic range of -80 dB normalized to $[0, 1]$. The green and red regions indicate the ROI and the background areas, respectively. The zoomed images correspond to the blue and yellow rectangles in the noisy image (5 CPWC) and the proposed method, respectively.

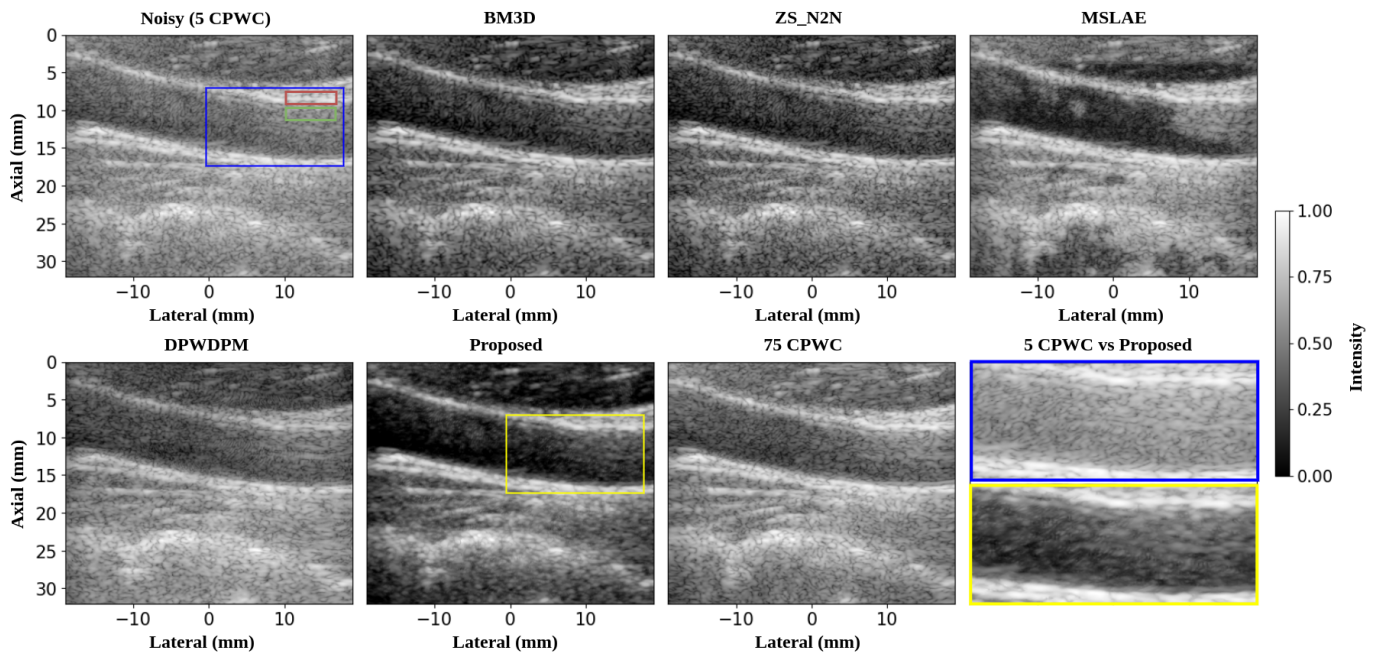


Fig. 4. Visual comparison of *in vivo* results (CL data). All images are displayed with a dynamic range of -80 dB normalized to $[0, 1]$. The green and red regions indicate the ROI and the background areas, respectively. The zoomed images correspond to the blue and yellow rectangles in the noisy image (5 CPWC) and the proposed method, respectively.

gCNR (0.90) and CNR (3.1) among all methods except the 75-angle compounded reference. Notably, these results are

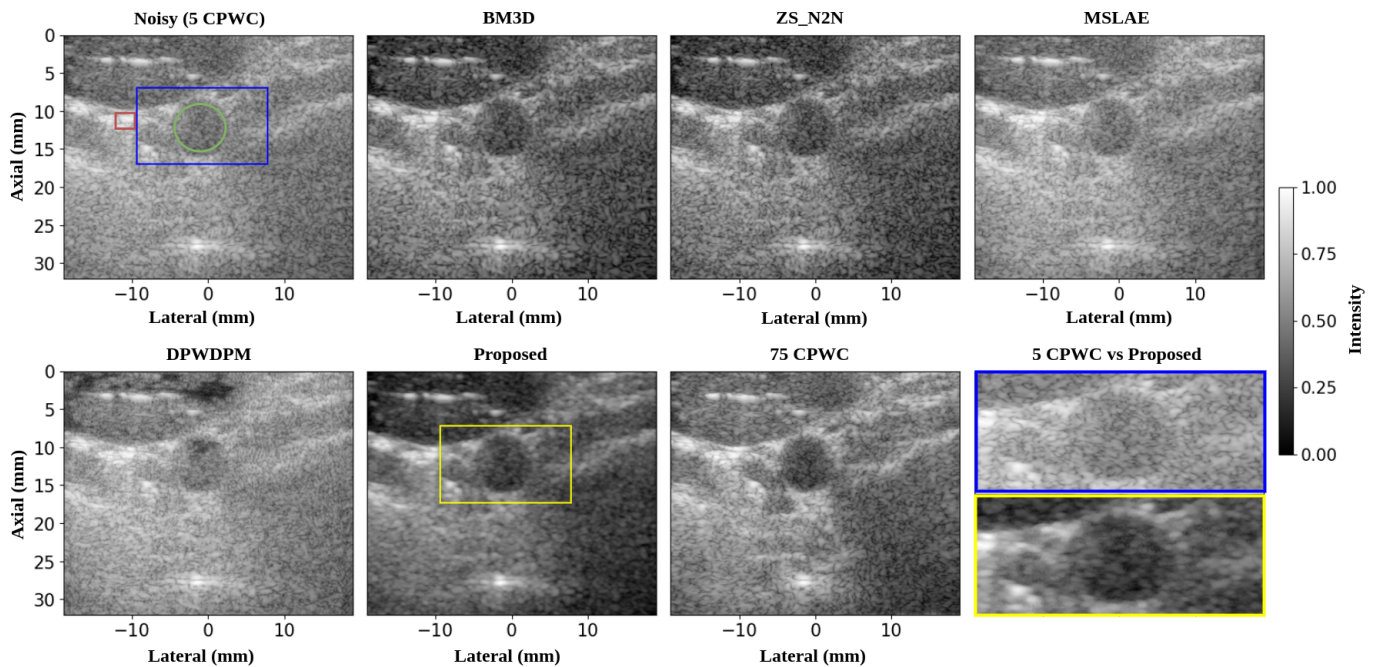


Fig. 5. Visual comparison of *in vivo* results (CC data). All images are displayed with a dynamic range of -80 dB normalized to $[0, 1]$. The green and red regions indicate the ROI and the background areas, respectively. The zoomed images correspond to the blue and yellow rectangles in the noisy image (5 CPWC) and the proposed method, respectively.

achieved without any retraining or adaptation to phantom data, highlighting the method’s resilience to domain shifts.

In *in vivo* studies, the framework maintains superior contrast and anatomical fidelity in both shallow and deep vascular targets. On the CL scan, the proposed method surpasses all baselines in both gCNR (0.87) and CNR (3.0), exceeding even the 75-angle reference. On the more challenging CC scan, it also yields the highest gCNR (0.80) and matches the top CNR (2.3), again without requiring any external training data. Visual inspections confirm sharper vessel boundaries and reduced background noise, particularly in low-contrast regions.

Another strength of our approach lies in its compact architecture. With fewer than 22k parameters and only two convolutional layers, the model maintains a lightweight structure that minimizes the chance of overfitting. Although the proposed method is not yet optimized for real-time denoising, future work will focus on enabling online deployment. To achieve this, we plan to pretrain the model on a diverse collection of plane wave datasets, allowing it to learn a robust initialization. With such a universal prior, the model would require only a few fine-tuning iterations on new data rather than the thousand of iterations it currently needs, substantially reducing the computational complexity.

The method’s ability to generalize across simulated, phantom, and *in vivo* domains highlights the potential for broader applicability across ultrasound imaging techniques such as focused imaging and synthetic aperture imaging. Extending the model to support various probe geometries, such as curved or phased arrays, is an area of future work.

Finally, while our method demonstrates stable and competitive results across different conditions, future studies should investigate its performance on larger and more diverse clinical

datasets. Furthermore, evaluating its impact on downstream clinical tasks, such as elastography, localization microscopy, or segmentation, would provide additional validation and insights into its practical utility.

VII. CONCLUSIONS

In this work, we presented a zero-shot denoising framework tailored for plane wave ultrasound imaging, leveraging paired subsets of compounded data to self-supervise a lightweight residual learning network. Our method requires no clean references or training datasets, making it practical for real-world deployment in clinical ultrasound systems. Through extensive experiments on simulation, experimental phantom, and *in vivo* datasets, we demonstrated that the proposed approach effectively reduces noise while preserving structural details and anatomical fidelity. The consistency and smoothing strategies further enhance robustness across varying imaging conditions. Despite its simplicity and low parameter count, our method competes favorably with supervised deep learning and classical denoising techniques, and in many cases, surpasses them. These results establish our approach as a promising, efficient solution for high-quality ultrasound reconstruction, particularly in settings with limited acquisition angles or a lack of training data.

REFERENCES

- [1] T. S. Stevens, F. C. Meral, J. Yu, I. Z. Apostolakis, J.-L. Robert, and R. J. van Sloun, “Dehazing ultrasound using diffusion models,” *IEEE Transactions on Medical Imaging*, pp. 1–1, 2024.
- [2] Y. Liu, N. Jiang, Z. Dai, and M. Zhang, “Advancing single-plane wave ultrasound imaging with implicit multiangle acoustic synthesis via deep learning,” *IEEE Trans. Ultrason. Ferroelectr. Freq. Control*, vol. 72, no. 4, pp. 479–497, Apr. 2025, doi: 10.1109/TUFFC.2025.3541113.

- [3] L. Eslami and B. Mohammadzadeh Asl, "Adaptive subarray coherence based post-filter using array gain in medical ultrasound imaging," *Ultrasonics*, vol. 126, p. 106808, 2022.
- [4] R. J. G. van Sloun, R. Cohen, and Y. C. Eldar, "Deep learning in ultrasound imaging," *Proceedings of the IEEE*, vol. 108, no. 1, pp. 11–29, 2020.
- [5] A. C. Luchies and B. C. Byram, "Deep neural networks for ultrasound beamforming," *IEEE Transactions on Medical Imaging*, vol. 37, no. 9, pp. 2010–2021, Sept. 2018, doi: 10.1109/TMI.2018.2809641.
- [6] S. Goudarzi, A. Asif, and H. Rivaz, "Ultrasound beamforming using MobileNetV2," in *Proc. IEEE Int. Ultrason. Symp. (IUS)*, Sep. 2020, pp. 1–4.
- [7] D. Xiao and A. C. H. Yu, "Beamforming-integrated neural networks for ultrasound imaging," *Ultrasonics*, vol. 145, p. 107474, 2025, doi: 10.1016/j.ultras.2024.107474.
- [8] A. Krull, T.-O. Buchholz, and F. Jug, "Noise2Void—Learning denoising from single noisy images," presented at the *IEEE/CVF Conf. Comput. Vis. Pattern Recognit.*, 2019, pp. 2129–2137.
- [9] J. Batson and L. Royer, "Noise2Self: Blind denoising by self-supervision," presented at the *Int. Conf. Mach. Learn.*, 2019, pp. 524–533.
- [10] T. Huang, S. Li, X. Jia, H. Lu, and J. Liu, "Neighbor2neighbor: Self-supervised denoising from single noisy images," in *Proc. IEEE/CVF Conf. Comput. Vis. Pattern Recognit. (CVPR)*, 2021, pp. 14781–14790.
- [11] M. Sharifzadeh, S. Goudarzi, A. Tang, H. Benali, and H. Rivaz, "Mitigating aberration-induced noise: A deep learning-based aberration-to-aberration approach," *IEEE Transactions on Medical Imaging*, pp. 1–1, 2024.
- [12] S. Goudarzi and H. Rivaz, "Deep ultrasound denoising without clean data," in *Medical Imaging 2023: Ultrasonic Imaging and Tomography*, vol. 12470, pp. 131–136, SPIE, Apr. 2023.
- [13] H. Cho, S. Park, J. Kang, and Y. Yoo, "Deep coherence learning: An unsupervised deep beamformer for high-quality single-plane-wave imaging in medical ultrasound," *Ultrasonics*, vol. 143, p. 107408, 2024.
- [14] C. Yu, F. Ren, S. Bao, Y. Yang, and X. Xu, "Self-supervised ultrasound image denoising based on weighted joint loss," *Digital Signal Processing*, vol. 162, p. 105151, 2025.
- [15] O. Mansour, P. I. Baykal, A. Katyal, D. Erdogmus, and V. K. Goyal, "Zero-Shot Noise2Noise: Efficient Image Denoising Without Any Data," in *IEEE/CVF Conf. Comput. Vis. Pattern Recognit. (CVPR)*, 2023, pp. 1–10.
- [16] P. Coupe, P. Hellier, C. Kervrann, and C. Barillot, "Nonlocal means-based speckle filtering for ultrasound images," in *IEEE Trans. Image Process.*, vol. 18, no. 10, pp. 2221–2229, Oct. 2009.
- [17] Y. Gan, E. Angelini, A. Laine, and C. Hendon, "BM3D-based ultrasound image denoising via brushlet thresholding," in *Proc. IEEE Int. Symp. Biomed. Imaging (ISBI)*, Brooklyn, NY, USA, 2015, pp. 667–670, doi: 10.1109/ISBI.2015.7163961.
- [18] G. Montaldo, M. Tanter, J. Bercoff, N. Benech, and M. Fink, "Coherent plane-wave compounding for very high frame rate ultrasonography and transient elastography," *IEEE Trans. Ultrason. Ferroelectr. Freq. Control*, vol. 56, no. 3, pp. 489–506, Mar. 2009, doi: 10.1109/TUFFC.2009.1067.
- [19] H. Rivaz, R. Zellars, G. Hager, G. Fichtinger, and E. Boctor, "9c-1 beam steering approach for speckle characterization and out-of-plane motion estimation in real tissue," in *Proc. IEEE Ultrason. Symp.*, Oct. 2007, pp. 781–784.
- [20] K. Hollman, K. Rigby, and M. O'Donnell, "Coherence factor of speckle from a multi-row probe," presented at the *IEEE Ultrason. Symp.*, 1999, pp. 1257–1260.
- [21] P.-C. Li and M.-L. Li, "Adaptive imaging using the generalized coherence factor," *IEEE Trans. Ultrason., Ferroelectr., Freq. Control*, vol. 50, no. 2, pp. 128–141, 2003.
- [22] C. Yang, Y. Jiao, T. Jiang, Y. Xu, and Y. Cui, "A united sign coherence factor beamformer for coherent plane-wave compounding with improved contrast," *Applied Sciences*, vol. 10, no. 7, p. 2250, 2020.
- [23] Y. Wang, C. Zheng, and H. Peng, "Dynamic coherence factor based on the standard deviation for coherent plane-wave compounding," *Comput. Biol. Med.*, vol. 108, pp. 249–262, 2019.
- [24] H. Asgariandehkordi et al., "Denoising plane wave ultrasound images using diffusion probabilistic models," *IEEE Trans. Ultrason., Ferroelectr., Freq. Control*, vol. 71, no. 11, pp. 1526–1539, Nov. 2024.
- [25] Y. Yang, H. Duan, and Y. Zheng, "Improved Transcranial Plane-Wave Imaging With Learned Speed-of-Sound Maps," *IEEE Trans. Med. Imaging*, vol. 43, no. 6, pp. 2191–2201, Jun. 2024, doi: 10.1109/TMI.2024.3358307.
- [26] Z. Zhou et al., "High spatial-temporal resolution reconstruction of plane-wave ultrasound images with a multichannel multiscale convolutional neural network," *IEEE Trans. Ultrason., Ferroelectr., Freq. Control*, vol. 65, no. 11, pp. 1983–1996, Nov. 2018.
- [27] L. S. Nguon et al., "Reconstruction for plane-wave ultrasound imaging using modified U-Net-based beamformer," *Comput. Med. Imaging Graph.*, vol. 98, p. 102073, 2022.
- [28] S. Goudarzi and H. Rivaz, "Deep reconstruction of high-quality ultrasound images from raw plane-wave data: A simulation and in vivo study," *Ultrasonics*, vol. 125, Sep. 2022, Art. no. 106778.
- [29] J.-Y. Lu, P.-Y. Lee, and C.-C. Huang, "Improving image quality for single-angle plane-wave ultrasound imaging with convolutional neural network beamformer," *IEEE Trans. Ultrason., Ferroelectr., Freq. Control*, vol. 69, no. 8, pp. 1326–1336, 2022.
- [30] D. Perdios et al., "Deep convolutional neural network for ultrasound image enhancement," presented at the *IEEE Int. Ultrason. Symp. (IUS)*, Oct. 2018, pp. 1–4.
- [31] H. Gupta et al., "Cnn-based projected gradient descent for consistent ct image reconstruction," *IEEE Transactions on Medical Imaging*, vol. 37, no. 6, pp. 1440–1453, 2018.
- [32] O. Huang, W. Long, N. Bottenus, M. Lerendegui, G. E. Trahey, S. Farsiu, and M. L. Palmeri, "Mimicknet, mimicking clinical image post-processing under black-box constraints," *IEEE Transactions on Medical Imaging*, vol. 39, no. 6, pp. 2277–2286, 2020.
- [33] A. K. Z. Tehrani and H. Rivaz, "Displacement estimation in ultrasound elastography using pyramidal convolutional neural network," *IEEE Transactions on Ultrasonics, Ferroelectrics, and Frequency Control*, vol. 67, no. 12, pp. 2629–2639, 2020.
- [34] D. Perdios, M. Vonlanthen, F. Martinez, M. Arditì, and J.-P. Thiran, "Cnn-based image reconstruction method for ultrafast ultrasound imaging," *IEEE Transactions on Ultrasonics, Ferroelectrics, and Frequency Control*, vol. 69, no. 4, pp. 1154–1168, 2022.
- [35] Z. Zhou et al., "Ultrafast plane wave imaging with line-scan-quality using an ultrasound-transfer generative adversarial network," *IEEE J. Biomed. Health Inform.*, vol. 24, no. 4, pp. 943–956, Apr. 2020.
- [36] J. Tang, B. Zou, C. Li, S. Feng, and H. Peng, "Plane-wave image reconstruction via generative adversarial network and attention mechanism," *IEEE Trans. Instrum. Meas.*, vol. 70, art. no. 4505115, pp. 1–15, 2021, doi: 10.1109/TIM.2021.3087819.
- [37] S. Goudarzi, A. Asif, and H. Rivaz, "Fast multi-focus ultrasound image recovery using generative adversarial networks," *IEEE Trans. Comput. Imag.*, vol. 6, pp. 1272–1284, 2020.
- [38] J. Ho, A. Jain, and P. Abbeel, "Denoising diffusion probabilistic models," in *Proc. NeurIPS*, vol. 33, pp. 6840–6851, 2020.
- [39] A. Q. Nichol and P. Dhariwal, "Improved denoising diffusion probabilistic models," in *Proc. Int. Conf. Mach. Learn. (ICML)*, 2021, pp. 8162–8171.
- [40] Z. Xiao, K. Kreis, and A. Vahdat, "Tackling the generative learning trilemma with denoising diffusion GANs," presented at the *Int. Conf. Learn. Represent. (ICLR)*, 2022.
- [41] H. Chung, B. Sim, and J. C. Ye, "Come-closer-diffuse-faster: Accelerating conditional diffusion models for inverse problems through stochastic contraction," in *Proc. IEEE/CVF Conf. Comput. Vis. Pattern Recognit. (CVPR)*, 2022, pp. 12413–12422.
- [42] X. Liu, C. Gong, and Q. Liu, "Flow straight and fast: Learning to generate and transfer data with rectified flow," arXiv preprint arXiv:2209.03003, 2022.
- [43] T. Liu et al., "Super-resolution reconstruction of ultrasound image using a modified diffusion model," *Phys. Med. Biol.*, vol. 69, no. 12, Art. no. 125026, Jun. 2024.
- [44] Y. Zhang, C. Huneau, J. Idier, and D. Mateus, "Diffusion reconstruction of ultrasound images with informative uncertainty," arXiv preprint arXiv:2310.20618, 2023.
- [45] T. S. Stevens, O. Nolan, O. Somphone, J. L. Robert, and R. J. van Sloun, "High volume rate 3D ultrasound reconstruction with diffusion models," arXiv preprint arXiv:2505.22090, 2025.
- [46] T. Chen, Y. Shi, Z. Zheng, B. Yan, J. Hu, X. X. Zhu, and L. Mou, "Ultrasound image-to-video synthesis via latent dynamic diffusion models," in *Proc. Int. Conf. Med. Image Comput. Comput.-Assist. Interv. (MICCAI)*, Cham, Switzerland: Springer Nature, Oct. 2024, pp. 764–774.
- [47] M. Domínguez, L. Mou, T. Chen, B. Yan, and X. X. Zhu, "Diffusion as sound propagation: Physics-inspired model for ultrasound image generation," in *Proc. Int. Conf. Med. Image Comput. Comput.-Assist. Interv. (MICCAI)*, Cham, Switzerland: Springer, 2024.
- [48] L. Zhu, J. Liu, Z. Liu, H. Zha, and S. Yan, "DiG: Scalable and efficient diffusion models with gated linear attention," in *Proc. IEEE/CVF Conf. Comput. Vis. Pattern Recognit. (CVPR)*, 2025.

- [49] J. Lehtinen, J. Munkberg, J. Hasselgren, S. Laine, T. Karras, M. Aittala, and T. Aila, "Noise2Noise: Learning image restoration without clean data," in *Proc. Int. Conf. Mach. Learn. (ICML)*, 2018, pp. 2965–2974.
- [50] J. Zhang, Q. He, Y. Xiao, H. Zheng, C. Wang, and J. Luo, "Ultrasound image reconstruction from plane wave radio-frequency data by self-supervised deep neural network," *Medical Image Analysis*, vol. 70, p. 102018, 2021.
- [51] Q. Kang, Q. Lao, J. Gao, J. Liu, H. Yi, B. Ma, X. Zhang, and K. Li, "Deblurring masked image modeling for ultrasound image analysis," *Medical Image Analysis*, vol. 97, p. 103256, 2024. doi: 10.1016/j.media.2024.103256.
- [52] Zhang, K., Zuo, W., Chen, Y., Meng, D., Zhang, L. "Beyond a Gaussian Denoiser: Residual Learning of Deep CNN for Image Denoising," in *IEEE Transactions on Image Processing*, 26(7), 3142-3155 (2017).
- [53] Chen, X., He, K., "Exploring simple siamese representation learning," in *Proceedings of the IEEE/CVF Conference on Computer Vision and Pattern Recognition (CVPR)*, pp. 15750–15758 (2021).
- [54] H. Liebgott, A. Rodriguez-Molares, F. Cervenansky, J. Jensen, and O. Bernard, "Plane-wave imaging challenge in medical ultrasound," in *2016 IEEE International Ultrasonics Symposium*, pp. 1–4, 2016.
- [55] Rodriguez-Molares, A., et al., "The generalized contrast-to-noise ratio: A formal definition for lesion detectability," in *IEEE Transactions on Ultrasonics, Ferroelectrics, and Frequency Control*, 67(4), 745–759 (2020).